This is a repository copy of *Martensitic twinning transformation mechanism in a metastable IVB element-based body-centered cubic high-entropy alloy with high strength and high work hardening rate*.

White Rose Research Online URL for this paper:
https://eprints.whiterose.ac.uk/195809/

Version: Accepted Version

Article:

eprints@whiterose.ac.uk
https://eprints.whiterose.ac.uk/

Twinning transformation induced ultrahigh work hardening capability in metastable high-entropy alloys

Abstract

With outstanding strength retention at elevated temperatures, refractory elements based high-entropy alloys (RHEAs) are promising candidates for high temperature applications. However, their practical application is limited by (early-onset plastic instability) poor malleability at ambient temperature, which results from a lack of deformation mechanisms and leads to premature failure. In this study, we report an entirely new plasticity mechanism the 'Twinning transformation induced plasticity' (TTIP) in metastable HEAs. It profoundly enhances the work hardening capability through transforming specific self-accommodation (SA) twinning to mechanical twinning in metastable RHEAs. Continuous twinning activation is inherited from the {351}<-211> type II SA α" (orthorhombic) twinning that occurs during the martensitic phase transformation which is capable to evolve into {351}<1-12> type I α" mechanical twinning and facilitates the formation of interpenetrating mechanical twins in both α" and β (body-centred cubic) phases. This synergistic effect of 'Transformation induced plasticity' (TRIP) and 'Twinning induced plasticity' (TWIP) enables ultrahigh work hardening rates to be sustained (2 – 11GPa) during deformation. We figure out that the phase stability affected SA type II α'' twinning invariant plane selection triggers this TTIP effect in martensite and further result in lattice correspond catalytic mechanical twinning nucleation in β phase. This discovery may not only provide a new strengthening mechanism which enables the metastable RHEAs to exhibit a superior combination of strength and ductility at ambient temperature, but also broadens the window towards designing high performance β→α" TRIP alloys.

Introduction

High entropy alloys (HEAs), consist of multiple constituent elements with near-equimolar fractions, have attracted significant interest due to their superior mechanical performance at both ambient and elevated temperatures [1-4]. The high configurational entropy of HEAs intrinsically enhances the thermal stability of solid solution phases at high temperature. This is particularly evident in a group of body-centric cubic (BCC) HEAs which primarily consists of group IV, V and VI refractory transition elements [5-8]. Exhibiting high strength, heat softening resistance and microstructural stability up to 1600℃, these refractory high entropy alloys (RHEAs) possess desirable characteristics for operating in the 1200℃ to 1600℃ temperature range, where conventional Co,Ni-based superalloys cannot be employed due to their relatively low melting points[5]. However, due to the nature of the BCC structure (not a close packed

structure) and the lack of deformation mechanisms, most of the BCC RHEAs exhibit a low work hardening response and poor ductility at ambient temperature[9–11], preventing their widespread usage.

The stress-induced martensite phase transformation has been proved effective at balancing the strength-ductility trade-off in metallic materials, *i.e.* Mn-Steel and metastable β-Ti alloys. It can be exploited to improve the work hardening capability, thereby enable large uniform elongation[12–15]. Similarly, the idea was successfully applied to group IVB element based BCC RHEAs through metastable engineering which exhibit the stress-induced β→α (hexagonal close packed)[16] and β→α''[17] phase transformation and possess an impressive combination of strength and ductility[16,17]. Nevertheless, the TRIP effect may insufficient to consistently sustain the work hardening in the entire duration of the deformation process. This leads to inhomogeneous localised deformation (*i.e.* necking) at early strain levels, which detrimentally affects the deformability and fracture resistance[18–21]. It becomes more apparent in similar TRIP-assisted alloys (*i.e.* TRIP β-Ti) where the work hardening capability enabled by TRIP is readily exhausted after yielding, resulting in a stress plateau during early deformation stages, while the resultant lack of strengthening leads to plastic instability during subsequent straining[22,23]. To alleviate this issue, concurrent TRIP and TWIP effects have been proven a desirable means for minimising the strength-ductility trade off, while maintaining high mechanical performance in FCC HEAs[24,25]. Serve as assisted strengthening mechanism, TWIP can offer continuous work hardening capability *via* progressively introducing coherent high angle grain boundaries (Twinning boundaries), leads to a dynamic Hall-Petch effect which reducing the mean free path for dislocation motion, can effectively delay the onset of plastic instability until higher strain/stress levels. However, such activation of apparently synchronous TRIP+TWIP effects has not yet been observed in metastable BCC RHEAs.

To obtain metastable BCC RHEAs with optimal combined TRIP and TWIP hardening, in the present study, emphasis is placed on promoting the 'self-accommodate' (SA) twinning in TRIP process. *I.e.* utilise the reorientation of stress-induced martensite variants to consistently sustain the dynamic hardening effect of TRIP. Driven by the stress-induced phase transformation, SA martensitic intervariants favour to arrange themselves into twinning structures to accommodate the overall volume change between martensite and austenite phases[26–29]. As is the case in mechanical twinning, the invariant interfaces of SA twinning always remain coherent[28,30,31] which enables the accommodation of localized stress-fields from accumulated dislocations in later strain. Known as sensitive to the stability of the austenite phase[12,19,20,32], we tuned the Ta(β-stabilizer) contents in IVB element based TiZrHfTa RHEAs[16] to investigate the effect of this SA twinning strengthening mechanism. Two model alloy, $(TiZrHf)_{85}Ta_{15}$ and $(TiZrHf)_{87}Ta_{13}$ were

synthesised for analysis. Ascribed to the massive SA twinning induced by TRIP in early deformation stage, the dense interfaces coherently mediate the localised stress and facilitate the strengthening effect inherited from phase transformation which leads to a pronounced work hardening capability in both compositions. Most interestingly, in $(TiZrHf)_{87}Ta_{13}$, where stress-induced α'', various SA type twins and deformation twinning modes are sequentially activated. We observed a so far undiscovered SA $\{351\}<-211>_{\alpha''}$ type II twinning-assisted strengthening mechanism. Utilising same lattice invariant plane, progressively increased deformation triggers $\{351\}<1-12>_{\alpha''}$ compound mechanical twinning to nucleate within the primary SA $\{351\}<-211>_{\alpha''}$ type II twinned α'' variants, which further expands and overtaking the type II twinned α'' lamella. Under continued straining, owing to the special lattice correspondence of this feature between β and α'' phase, catalytic twinning like feature was stimulated through α'' and β boundary. The resultant planar heterogeneous structure strongly impedes the dislocation motion and further contributes to an ultra-high work hardening capability, enabling high strength and ductility to be retained during the entire deformation process. A detailed infinitesimal deformation approach (IDA)[33,34] SA twinning calculations and EBSD/TEM analysis suggest this dynamic transformation twinning refinement behaviour may result from a re-selection of invariant plane for SA $<2-1-1>_{\alpha''}$ type II twinning modes. Without needs for large atomic shuffle but pure shear instead, this type II twinning to type I twinning transformation routine becomes an energetically favoured way to activate deformation twins in both α'' and β phase. This SA twinning strengthening mechanism was refer to as 'transformation twinning induced plasticity'(TTIP) by us which may not only maximise the effect of TRIP and TWIP mechanisms on ductilising the metastable RHEAs, but also offers a strong consistently dynamic strengthening method that could help alleviates the longstanding plastic instability in TRIP β-alloys designs.

Results

Mechanical properties and deformation analysis. The representative mechanical responses of $(TiZrHf)_{85}Ta_{15}$ and $(TiZrHf)_{87}Ta_{13}$ are shown in Fig. 1a, both work hardening rate and work hardening exponent curve are drawn to help distinguish the underlying hardening mechanism evolution. Both samples demonstrate a combination of high strength and ductility. Compared with $(TiZrHf)_{85}Ta_{15}$, the reduction of Ta content to 13% further lowers the β phase stability and increases the ultimate tensile strength (UTS) and the elongation to fracture up to 1310MPa and 25% respectively. The work hardening rate curves in Fig. 1a (mid panel) reveals this notable increase is attributed to the superb work hardening capability ($d\sigma_T/d\varepsilon_P$) of $(TiZrHf)_{87}Ta_{13}$ compared with $(TiZrHf)_{85}Ta_{15}$. The normalised work hardening rate

$((d\sigma_T/d\varepsilon_P)/G)$ of $(TiZrHf)_{87}Ta_{13}$ reaches 0.47G (where G is the bulk shear modulus), notably outperforms that achieved by high-performance TWIP and TRIP polycrystalline alloys[14,17,22-25,32-37]. Considering the maximum theoretical value of the normalised work hardening rate for dislocation solely assisted FCC alloys predicted from the Kocks–Mecking model is merely 0.05G[35], we can reasonably speculate that additional deformation mechanisms have been triggered to account for the pronounced work hardening capability. To accurate evaluate the underlying deformation mechanisms evolution in present alloys, three distinct hardening stages in $(TiZrHf)_{85}Ta_{15}$ and $(TiZrHf)_{87}Ta_{13}$ are highlighted in work hardening exponent curves (**Fig. 1a** bottom panel) while the corresponding phase constituents and structural evolution of $(TiZrHf)_{87}Ta_{13}$ are examined at 0%, 3%, 6% and 9% strain in Fig. 1b.
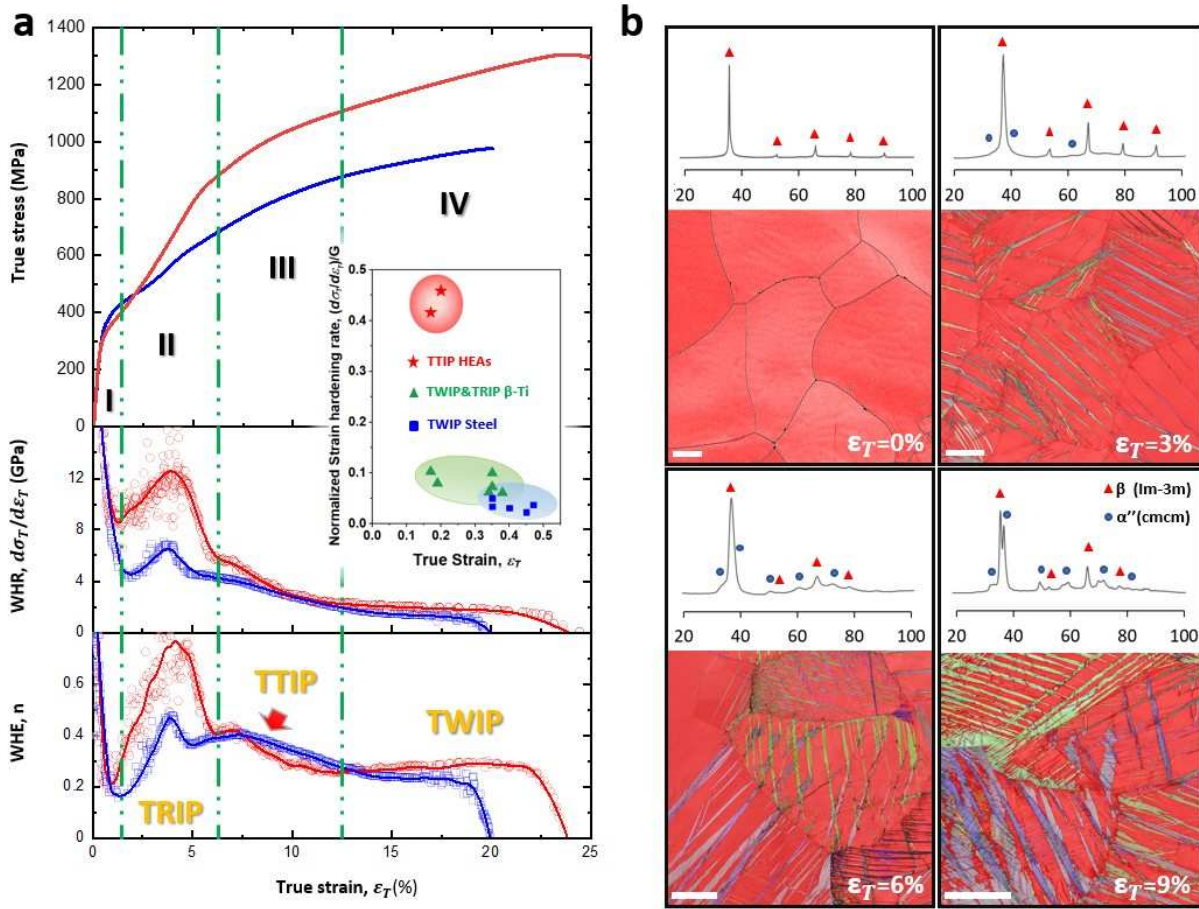

Figure. 1 mechanical properties of $(TiZrHf)_{85}Ta_{15}$ and $(TiZrHf)_{87}Ta_{13}$. (**a**) Tensile properties. The true stress vs. true strain curves of $(TiZrHf)_{85}Ta_{15}$ (blue) and $(TiZrHf)_{87}Ta_{13}$ (red) are shown in the top panel. The inset shows a comparison of the normalised work hardening rate $((d\sigma_T/d\varepsilon_P)/G)$ as a function of fracture strain between the present alloys and other high-performance titanium alloys and TWIP steels. The blue and green groups represent high strength Ti-alloys[17,22,36-38], TWIP steels[14,35,39] and TRIP-DP-HEA[24,25,40] respectively. Work hardening rate (WHR) curves of $(TiZrHf)_{85}Ta_{15}$ (blue) and $(TiZrHf)_{87}Ta_{13}$

Representative X-ray diffraction (XRD) and electron backscatter diffraction (EBSD) analyses (**Fig. 1b**) show only β phase present in the undeformed state (TiZrHf)$_{87}$Ta$_{13}$. When the deformation starts, in stage I, the work hardening rate drops dramatically where dislocation glide is attribute to the sole mechanism for accommodating the incoming stress; considering the critical resolved shear stress (CRSS) is not high enough to activate other deformation mechanisms[16,17]. During stage II, as straining progresses from 1.3% to 6%, a rapid rise in the work hardening rate which indicates the start of TRIP can be seen. In addition to the characteristic peaks of the β phase, a small peak corresponding to (020)$_{α''}$ is detected in the XRD spectrum of (TiZrHf)$_{87}$Ta$_{13}$ at 3% strain, where needle-like α'' martensite phase starts to form within the β grains(**Fig. 1b**). The indexed fraction of martensite phase is identified as 6.7%, while the activation of SA twinning is initiated. Through the construction of stereographic-projection figures for the α'' matrix and twinned α'' variants (EBSD twinning identification is presented in **Supplementary Fig. 1-2 and Note. II**), the primary triggered SA structure is confirmed to consist of two SA twinning systems, (111)$_{α''}$ type I and <-211>$_{α''}$ type II twins. The orientation relationship (OR) analysis indicates that the <-211>$_{α''}$ type II twinning system is utilising (**Supplementary Fig. 1**) a integral {351}$_{α''}$ invariant plane to accommodate the twinning shear. Further deformation successfully enhances the α'' percentage and produces a dual-phase microstructure with dense α'' lamellae embedded in the β matrix (**Fig. 1b, ε$_T$=6%**). With increasing strain, the martensite variants arrange themselves into a more complex SA morphology to overcome the volume misfit associated with the phase transformation. This confirms that the desired instability of the β phase has been successfully realised by fine-tuning of the Ta content, which enables the formation of stress-induced martensite and SA twinning, leading to the notable peaking of the work hardening rate at this stage. Moreover, besides the two SA twinning modes identified in 3% strained sample, a third α'' twinning system was indexed (**Fig. 1b, ε$_T$=6%**) and confirmed as an unusual (351)<1-12>$_{α''}$ compound twins. Starts from 6% strain, in stage III, where the early TRIP strengthening effect subsides, while dislocation glide and other deformation mechanisms continue to accommodate the extensive strain, maintaining the continuous strengthening up to higher strain levels. With an increasing fraction of β grain transformed into α'' phase, the (351)<1-12>$_{α''}$ compound twins percentage increased(**Supplementary Fig. 3**) and massive secondary twins are generated to accommodate the rising strain. This is seen after 9% strain, where a hierarchical heterogeneous lamellar structure has formed. In

bottom panel of Fig.1a, in comparison with $(TiZrHf)_{85}Ta_{15}$, the lightly revived work hardening exponent curve of $(TiZrHf)_{87}Ta_{13}$ after 12.5% strain (Stage IV) indicates other deformation mechanism has been activated that enables the work hardening capability to be sustained over a greater strain range. The ease of mechanical twinning activation in α'' grains, which has been firmly established through 'theory of the crystallography of deformation twinning' and EBSD-based studies by various authors[41-43], is postulated here as deformation products during deformation stages III and IV and contribute to the sustainable hardening capability after the TRIP effect subsides. Further TEM analysis were conducted in following sections to help distinguish the underneath deformation mechanisms during this stage.

Twinning evolution

The previous EBSD analysis shows that SA twinning plays leading role in maintaining work hardening during tensile straining. The presence of abundant secondary twins suggests that the heterogeneous structure may have also contributes to maintain the work hardening capability. To determine the underlying mechanism for activating massive concentrated secondary α'' twinning on primary martensite plate, transmission electron microscopy (TEM) was conducted on specimens with 5% and 10% strain. Concordant with the twinning OR identified from Fig. 1, besides type I $\{111\}_{α''}$ SA twin, the type II $<-211>_{α''}$ SA twin system is determined as another essential mode to accommodate the TRIP-induced volume misfit in the 5% strained specimen. The twinning plane of this type II $<-211>_{α''}$ twinning system is identified as an integral $\{351\}_{α''}$ plane in Fig. 2 where shows the TEM bright field image (**BFI**) of a primary type II $\{351\}<-211>_{α''}$ twin viewed along $[1-12]_{α''}$ zone axis. The twinning elements are determined from the selected area diffraction pattern (**SADP**) (**Fig. 2b**). Two sets of martensite diffraction spots, the matrix (M) and the twin(T) are observed coincided at $\{351\}_{α''}$ and, in the bright-field image(**Fig. 2a**), the twinning boundary is found perpendicular to the **g** vector of $(351)_{α''}$. Dark-field images (**DFI**) viewed along $(-111)_{α''M}$ and $(-111)_{α''T}$ reflections indicate that other deformation products may exist within the twinned α'' variant. In order to identify if the observed twinning is belongs to type II $<-211>_{α''}$ twin mode, the featured area was tilted to $[011]_{α''M}$ and $[001]_{α''M}$ zone axis where the observed lattice correspondence of matrix and twined variant $[011]_{α''M}//[100]_{α''T}$ and $[001]_{α''M}//[2-11]_{α''T}$ (**Supplementary Fig. 4-5**) matches $\{351\}<-211>_{α''}$ type II OR(**Supplementary Table. II**) well. From the SADP taken along $[100]_{α''M}//[011]_{α''T}$, the OR between the secondary α'' variant and primary type II twined variant is identified as type I $\{111\}_{α''}$ twin, while the dense laths observed across α'' bands are identified as anti-phase boundary (APB)-like stacking faults from DFI under two-beam conditions at

g*=110(**Fig. 2b(iii)**). Associated with martensitic transformation, the wavy APB nano-domains (**Fig. 2b(iii-iv)**) may serve as nucleation sites for new martensite variants to accommodate specific shear and enable generation of TTIP deformation products within the primary SA twins[44]. Spherical aberration corrected high-resolution TEM (HRTEM) shows that the {351}<-211>$_{\alpha''}$ type II twin exhibiting mirror symmetry against (351)$_{\alpha''}$ plane when viewed along [1-12]$_{\alpha''}$, as exemplified in Fig.2 (c-d). Result from the (001)<010>$_{\alpha''}$ instability, the atomic shuffled column can be seen in Fig. 2e, while not only exhibit in the matrix, same shuffled atomic column can also be found in the twined α'' variant on the adjacent (110)$_{\alpha''}$ plane, which indicates the mirror symmetry of this type II SA martenstic twin exist in both matrix and shuffled lattice. This extensive SA morphology observed in 5% strained sample suggest that the primary and secondary type I, type II twins are primarily account for the high work hardening capability during deformation stage II.
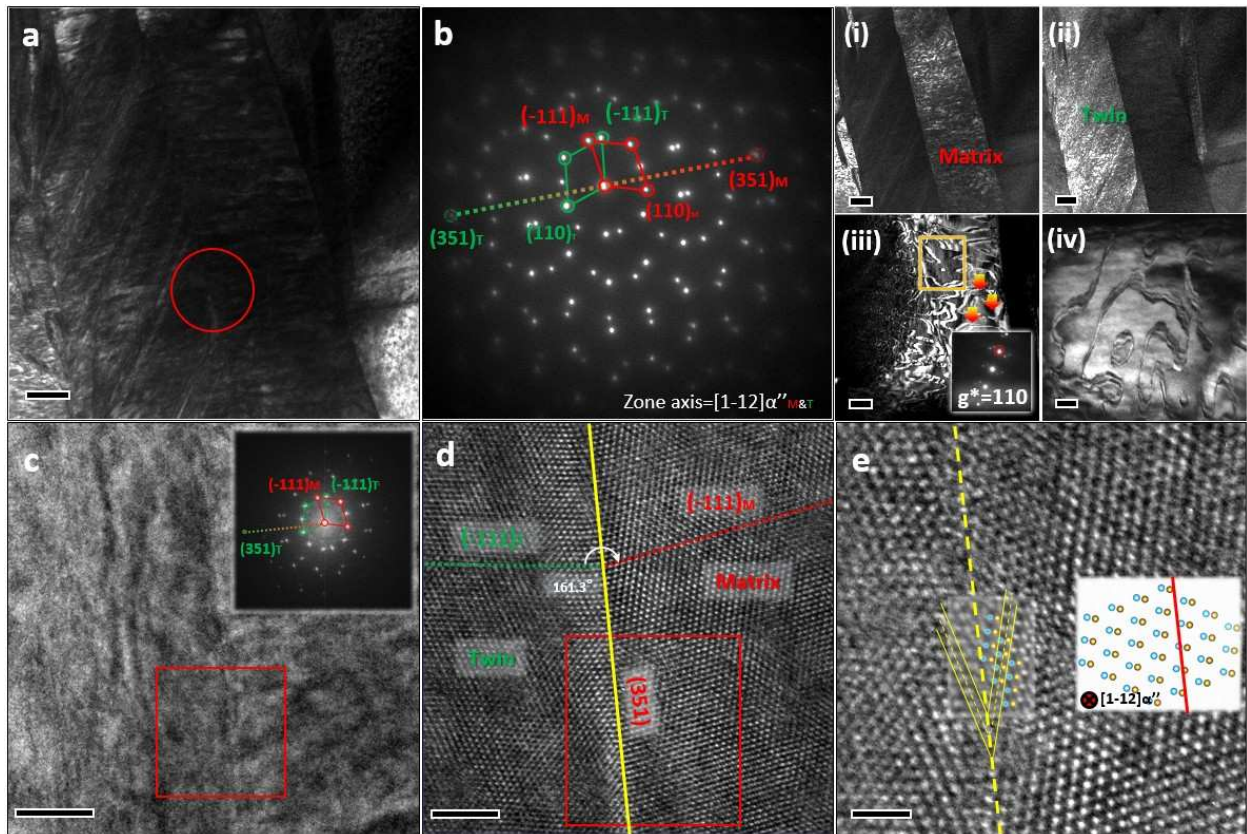

Figure. 2 TEM images of type II {351}<-211>$_{\alpha''}$ twinning in the deformed specimen at 5% strain. (**a**) Bright field image of the target area. (**b**) SADP from the twin boundary taken along the [1-12]$_{\alpha''}$ zone axis. The matrix and twin diffraction spots are marked with red and green circles respectively. **i.** DFI of the matrix and **ii.** of twin; **iii-iv.** Antiphase boundary (APB)-like stacking faults observed under a double beam condition where **g*=110**. (**c**) HRTEM taken along the [1-12]$_{\alpha''}$ zone axis from the twin feature. Inset is FFT of the imaged area. Matrix, twin variants reflections are marked with red, green circles respectively. (**d**) HRTEM of the twin boundary, the twinning plane and (-111)$_{M\&T}$ plane are marked with yellow line, red and green dash lines. (**e**)

Magnified HRTEM of the twinning boundary. Insets are wiener filtered image and simulated atomic configuration of the lattice viewed along $[1\text{-}12]_{\alpha''}$ zone axis. Blue and brown dots are indicate atoms at matrix and shuffled with $(001)<010>_{\alpha''}$ displacement respectively. Scale bars in a,b(i-iv), 200nm. Scale bar in c, 10nm. Scale bar in d, 2nm. Scale bar in e, 1nm.

The primary SA twinned α'' variants adopt a more complex arrangement to accommodate the additional deformation with further straining comes to 10%. In Fig. 3, TEM BFI shows a transformed type II $\{351\}<\text{-}211>_{\alpha''}$ SA twin structure, four involved martensite variants are designated as V1-4. SADPs taken from the origin and transformed $\{351\}<\text{-}211>_{\alpha''}$ twin boundary along $<112>_{\alpha''}$ and $<2\text{-}1\text{-}1>_{\alpha''}$ are shown in Fig. 3(b-c) and Supplementary Fig. 6-7 for comparison to illustrate the twinning structure evolution. The diffraction spots of α''V1 variant is first observed in Fig. 3b where the lattice correspondence $[10\text{-}1]_{\alpha''V1}//[\text{-}110]_{\alpha''V2}//[\text{-}112]_{\alpha''V3\&V4}$ is identified. While the OR between V3 and V4 can be easily identified from SADP as type II $(35\text{-}1)[2\text{-}11]_{\alpha''}$, to establish the origin of the V1 and V2, DFIs were taken from diffraction spots of the three α'' variants as shown in Fig. 3(d-f). Clearly, the DFIs presented in Fig. 3(d, e) indicate that the main α'' bands belong to V1, V3 and V4 respectively, while the thin laths separating them correspond to V2 variant. The sample was then tilted to $[2\text{-}1\text{-}1]_{\alpha''V1}$ zone axis to acquire further lattice correspondence information, as shown in Fig. 3c. Interestingly, there are only three sets of DPs indexed in Fig. 3c, while the V2's DP was missing. From current DPs in Fig. 3c, the lattice correspondence between V1,V3 and V4 was first confirmed from SADP as $[2\text{-}1\text{-}1]_{\alpha''V1}//[2\text{-}1\text{-}1]_{\alpha''V3}//[001]_{\alpha''V4}$ and $(351)_{\alpha''V1}//(351)_{\alpha''V3}//(130)_{\alpha''V4}$. Clearly, the OR between V1 and V3 can be assured as a type of $\{351\}_{\alpha''}$ twinning, when take $[10\text{-}1]_{\alpha''V1}//[\text{-}112]_{\alpha''V3}$ into consideration, the OR between V1 and V3 can be confirmed as $\{351\}<1\text{-}12>_{\alpha''}$ type I twinning. Accordingly, with V2 was observed between V1 and V3, by checking the possible lattice correspondence of martensite twinning in supplementary table.I, the OR between V1 and V2 was identified as type II $(351)[\text{-}211]_{\alpha''}$ twinning which helps explain why the DP for V2 is missing in Fig. 3c (Type II twinning operation: rotate 180 degree along $[\text{-}211]_{\alpha''}$, DP of V2 overlap with DPs of V1). Moreover, in same area of the specimen, we found this planar feature propagates through the adjacent α''-β interface and extends into the remnant β grain (**Supplementary Fig. 6c** yellow circled area). Most interestingly, the SADP obtained from the elongated laths in the β grain indicates that the coherently inherited α'' twin structures results in the formation of a $\{332\}<11\text{-}3>_{\beta}$ mechanical twin-like structure (**Supplementary Fig. 6b(iv))** in the β phase where the $(332)_{\beta}$ have lattice correspondence with $(351)_{\alpha''}$.
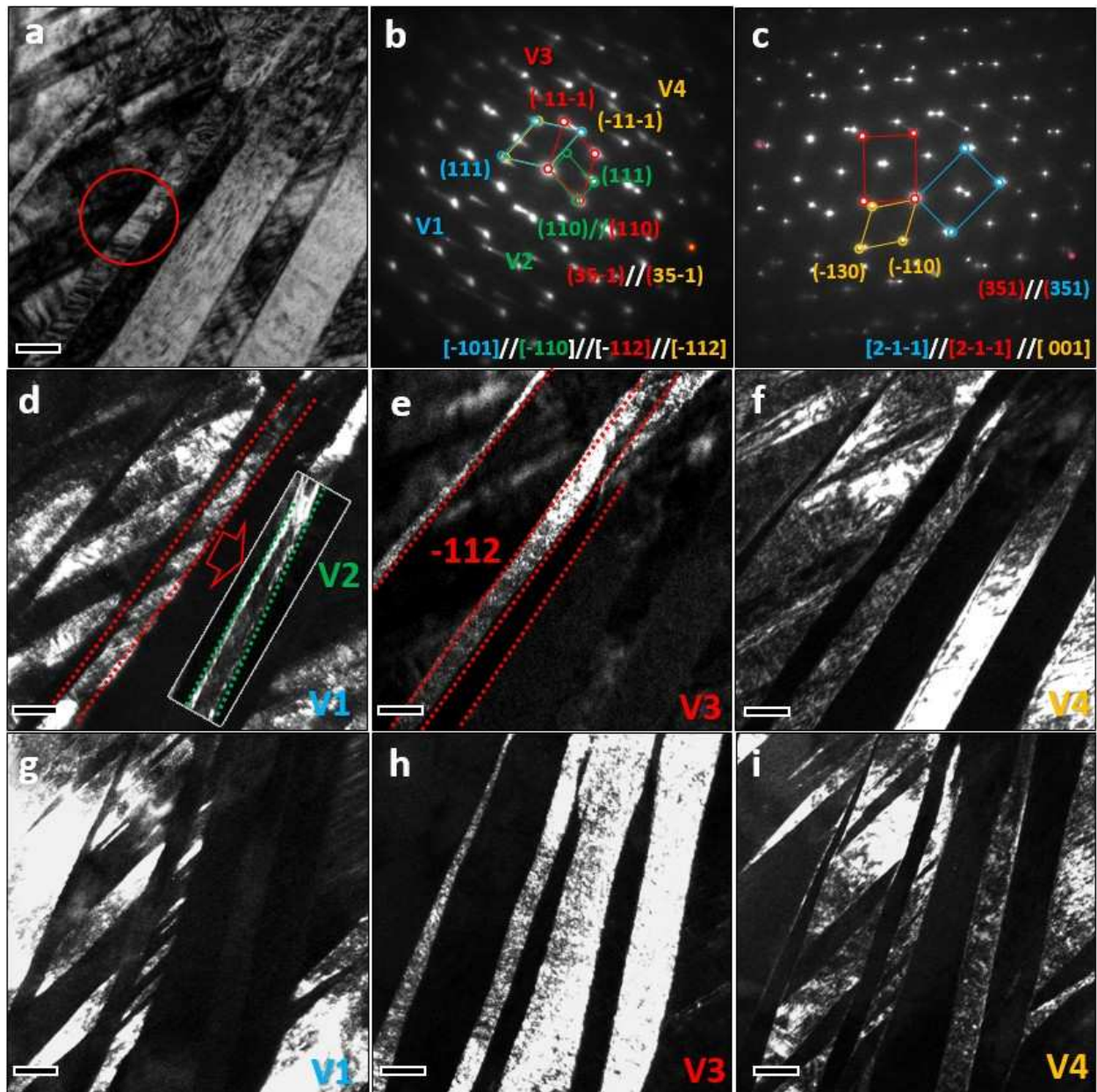
Figure. 3 TEM showing the microstructure evolution of SA type II {351}<-211>$_{\alpha''}$ twins. (a) BFI of the transformed SA {351}$_{\alpha''}$ twins after 10% strain. **(b-c)** SADP taken next to the twin boundary (red circle) along the [10-1]$_{\alpha''V1}$//[-110]$_{\alpha''V2}$//[-112]$_{\alpha''V3\&V4}$ and [2-11]$_{\alpha''V1-3}$//[001]$_{\alpha''V4}$ zone axis respectively. **(d-f)** DFI of four α'' variants imaged in Fig. 3b. **(g-i)** DFI of three α'' variants imaged in Fig. 3c. Scale bars, 50nm.

Atomic configuration of transformed {351}<-211> $_{\alpha''}$ type II twins

To understand the origin of the {351}<1-12>$_{\alpha''}$ type I twinning, based on previous analysis, the {351}<-211>$_{\alpha''}$ type II twinning structure was found to play a key role. Different with the α'' SA morphology

enabled via $\{111\}_{\alpha''}$ type I and $<-211>_{\alpha''}$ type II twinning in early deformation stage, from the OR analysis of Fig. 3, the $\{351\}<-1-12>_{\alpha''}$ twinning system was included as part of the conversion mechanism which transformed the primary $\{351\}<-211>_{\alpha''}$ type II twinned α''V2 variant into α''V3 along the $\{351\}_{\alpha''V2\&\alpha''V3}$ plane. To help understand this conversion mechanism, the feature in Fig. 3 was further analysed by HRTEM to characterise the underlying twinning transformation mechanism. Imaged along $[-112]_{\alpha''}$ zone axis, in conjunction with Fib. 3b, three sets of martensite variants diffraction reflections were captured from Fast Fourier transform (FFT) analysis of Fig. 4a. The lattice correspondence $[-101]_{V1}//[-110]_{V2}//[-112]_{V3}$(identified in Fig. 4b) was used to simulate the stereo-projection figure within the three variants (**Supplementary Figure. 5**). Locate within the narrow interfacial area between V1 and V3, the thin laths of V2 can be clearly observed in Fig.4b. With the spot of $(351)[1-12][2-1-1]_{\alpha''V1}$ superimposed on the $(351)[1-12][2-1-1]_{\alpha''V2}$ and $(351)[1-12][2-1-1]_{\alpha''V3}$(**Supplementary Figure. 5**), the $(351)_{\alpha''}$ plane was identified as a lattice invariant plane between V1, V2 and V3. While the OR between V1 and V2, V1 and V3 were confirmed as $(351)[2-1-1]_{\alpha''}$ type II twin and $(351)[1-12]_{\alpha''}$ type I twin, the OR between V2 and V3 can be then deduced. Illustrated by Fig. 4e, considering a crystallographic operation rotate V1 along $[2-1-1]_{\alpha''}$ 180 degree against $(351)_{\alpha''}$ plane result in a new variant V2(**Fig.4e(i)**) while another crystallographic operation produce mirror symmetry variant V3 of V1 against $(351)_{\alpha''}$ plane (**Fig. 4e(ii)**). The lattice of V2 and V1 only exhibiting mirror symmetry when viewed along $[1-12]_{\alpha''}$ zone axis(nearly perpendicular to $[-211]_{\alpha''}$) which indicates only twinning shear is required to transform V2 to V3(**Fig. 4e(iii-iv)**). Supported by Fig. 4d, in the same feature, when retiled to $[-211]_{\alpha''V1}//[-211]_{\alpha''V2}//[-211]_{\alpha''V3}$ the boundary between V1 and V2 vanished, whilst V1 and V3 exhibiting mirror symmetry against $(351)_{\alpha''}$ plane. Consequently, driving by the increasing stress, we believe the $\{351\}<2-1-1>_{\alpha''}$ twined V2 was progressively sheared into $\{351\}<1-12>_{\alpha''}$ twined V3 where only a small amount of type II twined α'' laths left as planar complexion structures between V3 and V1. Accordingly, by transforming the primary type II twined $\{351\}<2-1-1>_{\alpha''}$ variant to type I twined $\{351\}<1-12>_{\alpha''}$ variants, this observation suggests that a coherent twinning inheritance mechanism exist to enable the continuous deformation to be accommodated which may have acted as an additional work hardening source.
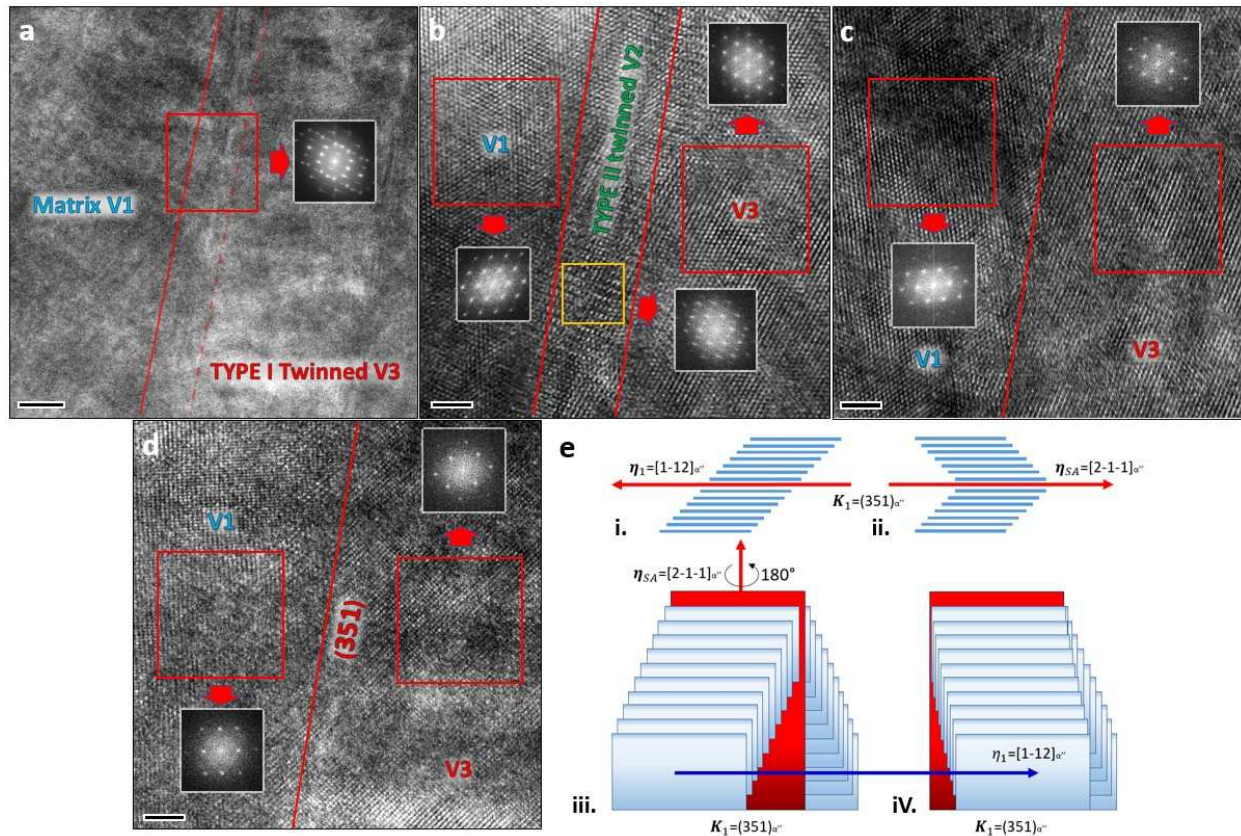
Figure. 4 HRTEM images of transformed {351}<-211>$_{\alpha''}$ twin boundary (**a**) Low mag HRTEM image of transformed {351}<-211>$_{\alpha''}$ type II twinning in a specimen strained to 10%. Insets are FFT of circled area. (**b**) Magnified image of circled area in (a) shows partially transformed {351}<-211>$_{\alpha''}$ type II twin structure. FFT of three martensite variants are shown in insets which exhibit reflections of [-101]$_{\alpha''V1}$, [-110]$_{\alpha''V2}$ and [-112]$_{\alpha''V3}$. (**c**) Fully transformed {351}<-211>$_{\alpha''}$ type II twin ({351}<1-12>$_{\alpha''}$ type I twin structure). FFT of two martensite variants are shown in insets which exhibit reflections of [-101]$_{\alpha''V1}$ and [-112]$_{\alpha''V3}$ (**d**). HRTEM image of same area in (c), acquired from [-211]$_{\alpha''}$ zone axis. FFT of two martensite variants are shown in insets which exhibit reflections of [2-1-1]$_{\alpha''V1}$ and [2-1-1]$_{\alpha''V3}$. (**e**)Schematic of {351}<2-1-1>$_{\alpha''}$ type II twin to {351}<1-12>$_{\alpha''}$ type I twin transformation. i-ii. projection of the type II (351)[2-1-1]$_{\alpha''}$ and type I (351)[1-12]$_{\alpha''}$ twin structure viewed along [2-1-1]$_{\alpha''}$ and [1-12]$_{\alpha''}$ direction respectively. iii. Lattice arrangement of the (351)[2-1-1]$_{\alpha''}$ type II twin. iv. Lattice arrangement of the (351)[2-1-1]$_{\alpha''}$ twin after shear along [1-12]$_{\alpha''}$ direction. Scar bar in (a), 20nm. Scar bars in (b-d), 2nm.
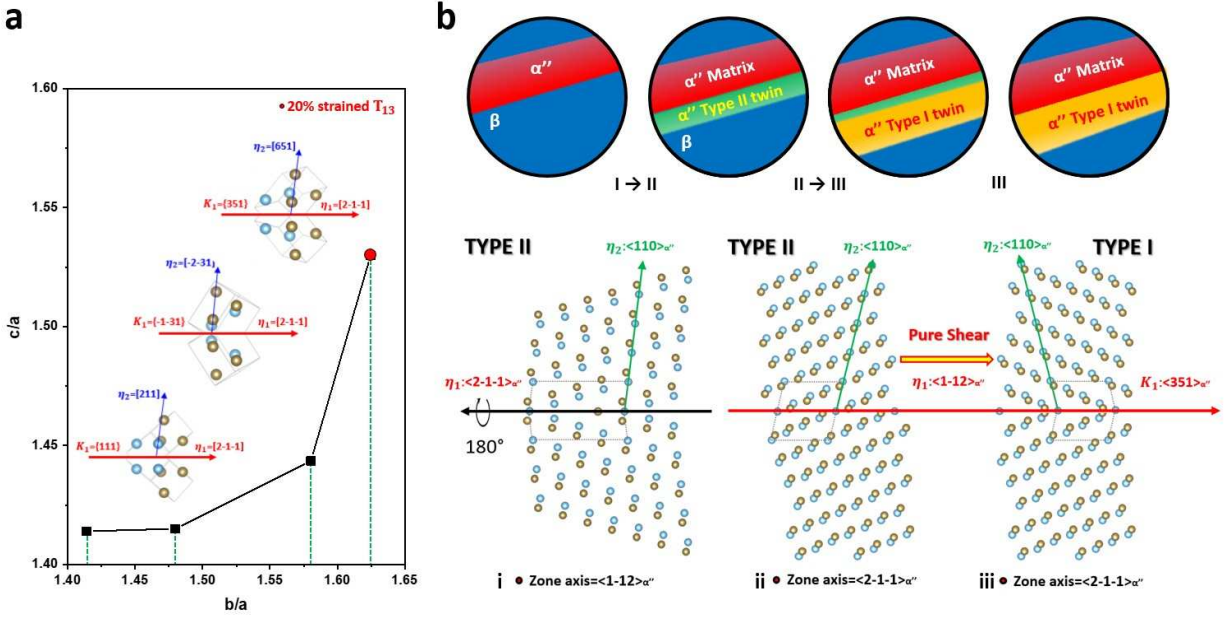
Discussion

Figure. 5 Martensitic type II to type I twinning evolution (**a**) The dependence of $<211>_{\alpha''}$ type II twinning modes selection on c/a and b/a ratios. The critical c/a and b/a ratios for activation of the three rational $<211>_{\alpha''}$ type II twinning modes are highlighted. (**b**) **I**. Initial formation of α'' (red). **II**. SA type II $\{351\}<-211>_{\alpha''}$ SA twinning (green) generate adjacent to the primary α''. **III**. mechanical $\{351\}<1-12>_{\alpha''}$ twins (orange) nucleate within SA twinned α'' variants and further overtake the SA twinned α'' variants. Bottom panel, Schematic representation of atomic movements associated with $\{351\}<-211>_{\alpha''}$ to $\{351\}<1-12>_{\alpha''}$ evolution. Blue and brown dots indicate atoms at matrix and shuffled with $(001)<010>_{\alpha''}$ displacement respectively. From left to right are projections of type II twin $\{351\}<-211>_{\alpha''}$ along $<1-12>_{\alpha''}$ and $<2-1-1>_{\alpha''}$, type I twin $\{351\}<1-12>_{\alpha''}$ along $<2-1-1>_{\alpha''}$ directions respectively.

The transformation twinning strengthening mechanism we discovered have combined the best of TRIP and TWIP in two aspects. The moderate volume difference between BCC and orthorhombic structures allows the α'' phase to form intricate arrangements by SA and mechanical twinning which minimise the overall shape change caused by phase transformation in early stage deformation. Such inter-variants conversion behaviour, in turn, dynamically refines the primary coarse grains into heterogeneous hierarchical structures (**Fig. 1b**) composed of different types of α'' twins which sustain the high work hardening capability enabled by TRIP into higher straining level through TWIP. In terms of α'' SA twinning activation, different with the previous infinitesimal invariant plane expression of SA type II $<-211>_{\alpha''}$ twinning obtained by infinitesimal deformation approach(IDA)[45], we discovered a special SA type II $<-211>_{\alpha''}$ twinning mode which take integral $\{351\}_{\alpha''}$ as twinning plane. Lattice correspond to the $\{332\}_{\beta}$ plane (well-known for twinning plane of $\{332\}<11-3>_{\beta}$ mechanical twinning in β phase), this special lattice correspondence allows type I $\{351\}[1-12]_{\alpha''}$ twinning nucleate within the SA type II $\{351\}[2-1-1]_{\alpha''}$

twinned variant which further leads to a twinning transmission like structure propagate through the α''-β boundary as $\{332\}<11\text{-}3>_\beta$ mechanical twin and contribute to the pronounced work hardening capability. While further explanation is clearly needed, in following we discuss the twinning evolution process in a coherent manner.

Induced by the martensitic phase transformation, in many alloy systems (i.e., TiNi and TiNb) SA twins are generated as accommodation to the volume misfit between martensite and austenite phase. The twinning elements of different SA twins are used to be calculated by the Bilby-Crocker[46] deformation twinning theory and IDA[34,45], where in α'' the general solution of SA twins includes $\{011\}_{\alpha''}$ compound twin, $\{111\}_{\alpha''}$ type I and $<\text{-}211>_{\alpha''}$ type II twins; in monolithic phase(B19') of TiNi alloy is type II $<011>_{B19'}$ twin. Although in most cases only irrational twin planes were calculated for type II twins, the real lattice arrangement are actually confirmed as composed of continuous rational twin plane segment (i.e., $\{111\}_{B19'}$ in type II $<011>_{B19'}$ twin)[47,48]. In current situation, when substitute into the α'' lattice parameters of the fully deformed $(TiZrHf)_{87}Ta_{13}$ specimen, the solution of twinning elements for $<\text{-}211>_{\alpha''}$ type II SA twinning mode remain irrational. However, taking the ratio of b/a and c/a as variables, we found three rational solutions (**listed in Supplementary table. III**) exists to serve as lattice invariant strain of SA type II $<\text{-}211>_{\alpha''}$ twin. In consistent with our result and observation of the $\{351\}<\text{-}211>_{\alpha''}$ twin, the $\{13\text{-}1\}<\text{-}211>_{\alpha''}$ mode has also been reported in Ti-Nb binary system[49] which encourage the deduction that lower c/a and b/a ratios during the early phase transformation stage allows the SA type II $<\text{-}211>_{\alpha''}$ twin to select different rational plane to accommodate lattice invariant strain. The low magnitude of shear vector required for the rational SA type II $<\text{-}211>_{\alpha''}$ twin modes (**see Supplementary table. II**) results in their activation at the early deformation stage to accommodate the incoming stress rather than mechanical twins. In the case of metastable $(TiZrHf)_{100\text{-}x}Ta_x$ RHEAs, the lowered β phase stability (when Ta=13%~15%. at%) results in different displaced $\{001\}<010>_{\alpha''}$ atomic shuffle[50] which further affects the b/a and c/a ratio variance during deformation, thereby leads to distinct TTIP effect in work hardening response.

The implications obtained from the IDA result is summarised in a schematic illustration shows in Fig. 5b for a detailed explanation of the observed TTIP mechanism. After yielding, the β → α'' martensite phase transformation (TRIP) is triggered as the primary deformation mechanism (**Step I**). To prevent the overall volume change and balance the local stress, the readily activated SA type twinning is predominant in following deformation stage (**Step II**) where the resultant high density SA type I $\{111\}_{\alpha''}$ and type II $\{\text{-}211\}_{\alpha''}$ SA twined α'' variants make the main contribution to the first peak in work hardening curves (**Fig.**

1a). During Step II, a special SA $\{351\}<-211>_{\alpha''}$ type II twin is activated as the precursor for the start of Step III, whereby TTIP takes effect and mediates the transition between TRIP and TWIP. Same as other martensitic mechanical twinning, the biggest obstacle for the direct activation of $\{351\}<1-12>_{\alpha''}$ mechanical twinning is the atomic shuffle required to move one-half of the atoms to appropriate twinned lattice sites after twinning shear(see **Supplementary figure. 9**)[41,51]. However, by nucleated within the primary $\{351\}<-211>_{\alpha''}$ type II twinned variant, the requirement of atomic shuffle vanished as shown in Fig. 5b(i-iii) where pure twinning shear is enough to transfer primary $\{351\}<-211>_{\alpha''}$ type II twinned variant into $\{351\}<1-12>_{\alpha''}$ compound twinned variant. Therefore, when TRIP effect subsided, the progressive increased strain satisfied the higher energy needed and encouraged the activation of $\{351\}<1-12>_{\alpha''}$ mechanical twinning. Utilising same twinning plane as highlighted in Fig. 5, the energetically favourable mechanical twin transformation occurs in the primary $(351)[-211]_{\alpha''}$ type II twins along $(351)[1-12]_{\alpha''}$ to accommodate further deformation. During the SA twin to mechanical twin transformation in Step III, the $\{351\}<-211>_{\alpha''}$ twined variant is progressively transformed into secondary $\{351\}<1-12>_{\alpha''}$ twined variant (Fig. 5b) where the special lattice correspondence between $(351)<1-12>_{\alpha''}$ and $(332)<1-13>_{\beta}$ allowing this transformed twinning structure propagated into the adjacent β phase in the form of catalytic $\{332\}<11-3>_{\beta}$ mechanical twinning-like structure (**Supplementary Fig. 6b(iv)**). This has alleviated the accumulated local stress at the α'' transformed twin/β boundary junction in a coherent manner and further attribute to the dynamic work hardening capability of the retained β grain in the last deformation stage. The three twinning transformation steps discussed above constitute the mechanism of TTIP. Need to notice, lattice correspond to $\{121\}_{\beta}$, the TTIP effect is also capable to be activated through $\{13-1\}<2-1-1>_{\alpha''}$ type II twin along $\{13-1\}<1-12>_{\alpha''}$ direction and further activate nucleation of $\{121\}<1-11>_{\beta}$ twin in β phase.

In summary, the innovative concept of transformation twinning induced plasticity (TTIP) is presented for the first time based on the experimental evidence we discovered. Outstanding work hardening capability is enabled through activation of the TTIP effect *via* a special $\{351\}<-211>_{\alpha''}$ type II SA twinning system. Owing special lattice correspondence with twinning system in β phase, the resultant deformation products coherently extends through α''/β boundary, provides essential mechanism to alleviate the localised stresses generated adjacent to α'' twinning/β boundary junction. Resultant dense tangled hierarchical gradient twins spanning from the µm scale primary α'' to nm scale SA twins and mechanical α'' twins have provided profuse low-misfit interfaces to accommodate the deformation. The intricate twinning network further restrict the available path for the glide of dislocations and triggers a dynamic Hall-Petch effect in $(TiZrHf)_{87}Ta_{13}$ RHEAs which consequently enables a balance of high strength

and ductility with a pronounced work hardening capability in ambient temperatures. The sequential activated SA twinning modes are rationalized, relative to the β phase stability, twinning modes selection in α'' phase can be influenced by compositional tailoring which provides an essential implication in utilise this SA twinning strengthening mechanism. The importance of TTIP is self-evident, heretofore, it provides an undiscovered transition pathway between TRIP and TWIP mechanism through SA to mechanical twins transformation which can be feasibly applied on tuning and optimizing alloy performance in many other metallic material that exhibit the BCC-HCP athermal phase transformation during deformation (*e.g.* Steels, Mg alloys, Zr alloys, *etc.*).

Reference

1. Gludovatz, B. *et al.* A fracture-resistant high-entropy alloy for cryogenic applications. *Science (80-.).* (2014). doi:10.1126/science.1254581

2. Yeh, J. W. *et al.* Nanostructured high-entropy alloys with multiple principal elements: Novel alloy design concepts and outcomes. *Adv. Eng. Mater.* (2004). doi:10.1002/adem.200300567

3. Lei, Z. *et al.* Enhanced strength and ductility in a high-entropy alloy via ordered oxygen complexes. *Nature* (2018). doi:10.1038/s41586-018-0685-y

4. Yang, T. *et al.* Multicomponent intermetallic nanoparticles and superb mechanical behaviors of complex alloys. *Science (80-.).* (2018). doi:10.1126/science.aas8815

5. Senkov, O. N., Miracle, D. B., Chaput, K. J. & Couzinie, J. P. Development and exploration of refractory high entropy alloys - A review. *Journal of Materials Research* (2018). doi:10.1557/jmr.2018.153

6. Juan, C. C. *et al.* Enhanced mechanical properties of HfMoTaTiZr and HfMoNbTaTiZr refractory high-entropy alloys. *Intermetallics* (2015). doi:10.1016/j.intermet.2015.03.013

7. Wu, Y. D. *et al.* A refractory Hf 25 Nb 25 Ti 25 Zr 25 high-entropy alloy with excellent structural stability and tensile properties. *Mater. Lett.* (2014). doi:10.1016/j.matlet.2014.05.134

8. Chen, J. *et al.* A review on fundamental of high entropy alloys with promising high–temperature properties. *Journal of Alloys and Compounds* (2018). doi:10.1016/j.jallcom.2018.05.067

9. Senkov, O. N., Wilks, G. B., Scott, J. M. & Miracle, D. B. Mechanical properties of Nb25Mo25Ta25W25 and V20Nb20Mo20Ta20W20 refractory high entropy alloys. *Intermetallics* (2011). doi:10.1016/j.intermet.2011.01.004

10. Senkov, O. N., Senkova, S. V. & Woodward, C. Effect of aluminum on the microstructure and properties of two refractory high-entropy alloys. *Acta Mater.* (2014). doi:10.1016/j.actamat.2014.01.029

11. Zou, Y., Maiti, S., Steurer, W. & Spolenak, R. Size-dependent plasticity in an Nb25Mo25Ta 25W25 refractory high-entropy alloy. *Acta Mater.* (2014). doi:10.1016/j.actamat.2013.11.049

12. Turteltaub, S. & Suiker, A. S. J. Transformation-induced plasticity in ferrous alloys. *J. Mech. Phys. Solids* (2005). doi:10.1016/j.jmps.2005.03.004

13. Transformation induced plasticity. *Adv. Mater. Process.* (2005). doi:10.1115/1.3101930

14. Ma, Y., Song, W. & Bleck, W. Investigation of the microstructure evolution in a Fe-17Mn-1.5Al-0.3C steel via in situ synchrotron X-ray diffraction during a tensile test. *Materials (Basel).* (2017). doi:10.3390/ma10101129

15. Tran, J. Titanium by design: Trip titanium alloy. *ProQuest Diss. Theses Glob.* (2009).

16. Huang, H. *et al.* Phase-Transformation Ductilization of Brittle High-Entropy Alloys via

Metastability Engineering. *Adv. Mater.* (2017). doi:10.1002/adma.201701678

17. Lilensten, L. *et al.* Design and tensile properties of a bcc Ti-rich high-entropy alloy with transformation-induced plasticity. *Mater. Res. Lett.* (2017). doi:10.1080/21663831.2016.1221861

18. Gutierrez-Urrutia, I. & Raabe, D. Grain size effect on strain hardening in twinning-induced plasticity steels. *Scr. Mater.* (2012). doi:10.1016/j.scriptamat.2012.01.037

19. Allain, S., Chateau, J. P., Dahmoun, D. & Bouaziz, O. Modeling of mechanical twinning in a high manganese content austenitic steel. *Mater. Sci. Eng. A* (2004). doi:10.1016/j.msea.2004.05.038

20. Pierce, D. T. *et al.* The influence of manganese content on the stacking fault and austenite/ε-martensite interfacial energies in Fe-Mn-(Al-Si) steels investigated by experiment and theory. *Acta Mater.* (2014). doi:10.1016/j.actamat.2014.01.001

21. Qin, B. & Bhadeshia, P. H. K. D. H. Crystallography of TWIP Steel. *Grad. Inst. Ferr. Technol.* (2007). doi:10.1002/bmb.15

22. Sun, F. *et al.* A new titanium alloy with a combination of high strength, high strain hardening and improved ductility. *Scr. Mater.* (2015). doi:10.1016/j.scriptamat.2014.09.005

23. Sun, F. *et al.* Investigation of early stage deformation mechanisms in a metastable β titanium alloy showing combined twinning-induced plasticity and transformation-induced plasticity effects. *Acta Mater.* (2013). doi:10.1016/j.actamat.2013.07.019

24. Li, Z., Tasan, C. C., Springer, H., Gault, B. & Raabe, D. Interstitial atoms enable joint twinning and transformation induced plasticity in strong and ductile high-entropy alloys. *Sci. Rep.* (2017). doi:10.1038/srep40704

25. Li, Z., Tasan, C. C., Pradeep, K. G. & Raabe, D. A TRIP-assisted dual-phase high-entropy alloy: Grain size and phase fraction effects on deformation behavior. *Acta Mater.* (2017). doi:10.1016/j.actamat.2017.03.069

26. Bhattacharya, K. Self-accommodation in martensite. *Arch. Ration. Mech. Anal.* (1992). doi:10.1007/BF00375026

27. Chai, Y. W., Kim, H. Y., Hosoda, H. & Miyazaki, S. Self-accommodation in Ti-Nb shape memory alloys. *Acta Mater.* (2009). doi:10.1016/j.actamat.2009.04.051

28. Adachi, K., Perkins, J. & Wayman, C. M. Type II twins in self-accommodating martensite plate variants in a CuZnAl shape memory alloy. *Acta Metall.* (1986). doi:10.1016/0001-6160(86)90150-1

29. Inamura, T., Hosoda, H., Young Kim, H. & Miyazaki, S. Antiphase boundary-like stacking fault in α″-martensite of disordered crystal structure in β-titanium shape memory alloy. *Philos. Mag.* (2010). doi:10.1080/14786435.2010.489889

30. Saburi, T. & Wayman, C. M. Crystallographic similarities in shape memory martensites. *Acta Metall.* (1979). doi:10.1016/0001-6160(79)90186-X

31. Microstructure of martensite: why it forms and how it gives rise to the shape-memory effect. *Choice Rev. Online* (2013). doi:10.5860/choice.41-6554

32. Fischer, F. D. *et al.* New view on transformation induced plasticity (TRIP). *Int. J. Plast.* (2000).

doi:10.1016/S0749-6419(99)00078-9

33. Kato, M. & Shibata-Yanagisawa, M. Infinitesimal deformation approach of the phenomenological crystallographic theory of martensitic transformations. *J. Mater. Sci.* (1990). doi:10.1007/BF00544207

34. Liang, Y., Kato, H., Taya, M. & Mori, T. Infinitesimal approach to the crystallography of martensitic transformation: application to Ni-Ti. *Scr. Mater.* (2000). doi:10.1016/S1359-6462(00)00465-6

35. Mecking, H. & Kocks, U. F. Kinetics of flow and strain-hardening. *Acta Metall.* (1981). doi:10.1016/0001-6160(81)90112-7

36. Brozek, C. *et al.* A β-titanium alloy with extra high strain-hardening rate: Design and mechanical properties. *Scr. Mater.* (2016). doi:10.1016/j.scriptamat.2015.11.020

37. Ji, X., Emura, S., Min, X. & Tsuchiya, K. Strain-rate effect on work-hardening behavior in β-type Ti-10Mo-1Fe alloy with TWIP effect. *Mater. Sci. Eng. A* (2017). doi:10.1016/j.msea.2017.09.055

38. Ahmed, M., Wexler, D., Casillas, G., Ivasishin, O. M. & Pereloma, E. V. The influence of β phase stability on deformation mode and compressive mechanical properties of Ti-10V-3Fe-3Al alloy. *Acta Mater.* (2015). doi:10.1016/j.actamat.2014.10.043

39. Grässel, O., Krüger, L., Frommeyer, G. & Meyer, L. W. High strength Fe-Mn-(Al, Si) TRIP/TWIP steels development - properties - application. *Int. J. Plast.* (2000). doi:10.1016/S0749-6419(00)00015-2

40. Li, Z., Pradeep, K. G., Deng, Y., Raabe, D. & Tasan, C. C. Metastable high-entropy dual-phase alloys overcome the strength-ductility trade-off. *Nature* (2016). doi:10.1038/nature17981

41. Tobe, H., Kim, H. Y., Inamura, T., Hosoda, H. & Miyazaki, S. Origin of {3 3 2} twinning in metastable β-Ti alloys. *Acta Materialia* (2014). doi:10.1016/j.actamat.2013.10.048

42. Zhang, X., Wang, W. & Sun, J. Formation of {332} ⟨113⟩ βtwins from parent {130} ⟨310⟩ α″plastic twins in a full α″ Ti-Nb alloy by annealing. *Mater. Charact.* (2018). doi:10.1016/j.matchar.2018.09.034

43. Zhang, J., Tasan, C. C., Lai, M. J., Dippel, A. C. & Raabe, D. Complexion-mediated martensitic phase transformation in Titanium. *Nat. Commun.* (2017). doi:10.1007/s00117-017-0224-0

44. Lee, S., Park, C., Hong, J. & Yeom, J. taek. The Role of Nano-domains in {1−011} Twinned Martensite in Metastable Titanium Alloys. *Sci. Rep.* (2018). doi:10.1038/s41598-018-30059-8

45. Inamura, T. *et al.* Composition dependent crystallography of α″-martensite in Ti-Nb-based β-titanium alloy. *Philos. Mag.* (2007). doi:10.1080/14786430601003874

46. Bilby, B. A. & Crocker, A. G. The Theory of the Crystallography of Deformation Twinning. *Proc. R. Soc. A Math. Phys. Eng. Sci.* (1965). doi:10.1098/rspa.1965.0216

47. Xie, Z. L. & Liu, Y. HRTEM study of (011) type II twin in NiTi shape memory alloy. *Philos. Mag.* (2004). doi:10.1080/14786430412331283596

48. Mohammed, A. S. K. & Sehitoglu, H. Modeling the interface structure of type II twin boundary in B19′ NiTi from an atomistic and topological standpoint. *Acta Mater.* (2020). doi:10.1016/j.actamat.2019.10.048

49.	Tobe, H. *et al.* Effect of Nb content on deformation behavior and shape memory properties of Ti-Nb alloys. *J. Alloys Compd.* (2013). doi:10.1016/j.jallcom.2012.02.023

50.	Nii, Y., Arima, T. H., Kim, H. Y. & Miyazaki, S. Effect of randomness on ferroelastic transitions: Disorder-induced hysteresis loop rounding in Ti-Nb-O martensitic alloy. *Phys. Rev. B - Condens. Matter Mater. Phys.* (2010). doi:10.1103/PhysRevB.82.214104

51.	Crocker, A. G. Twinned martensite. *Acta Metall.* (1962). doi:10.1016/0001-6160(62)90056-1

52.	Perl, J., Shin, J., Schümann, J., Faddegon, B. & Paganetti, H. TOPAS: An innovative proton Monte Carlo platform for research and clinical applications. *Med. Phys.* (2012). doi:10.1118/1.4758060

53.	Klinger, M. & Jäger, A. Crystallographic Tool Box (CrysTBox): automated tools for transmission electron microscopists and crystallographers . *J. Appl. Crystallogr.* (2015). doi:10.1107/s1600576715017252

54.	Gu, X.-F., Furuhara, T. & Zhang, W.-Z. PTCLab : free and open-source software for calculating phase transformation crystallography . *J. Appl. Crystallogr.* (2016). doi:10.1107/s1600576716006075

Supplementary information

Supplementary Figures
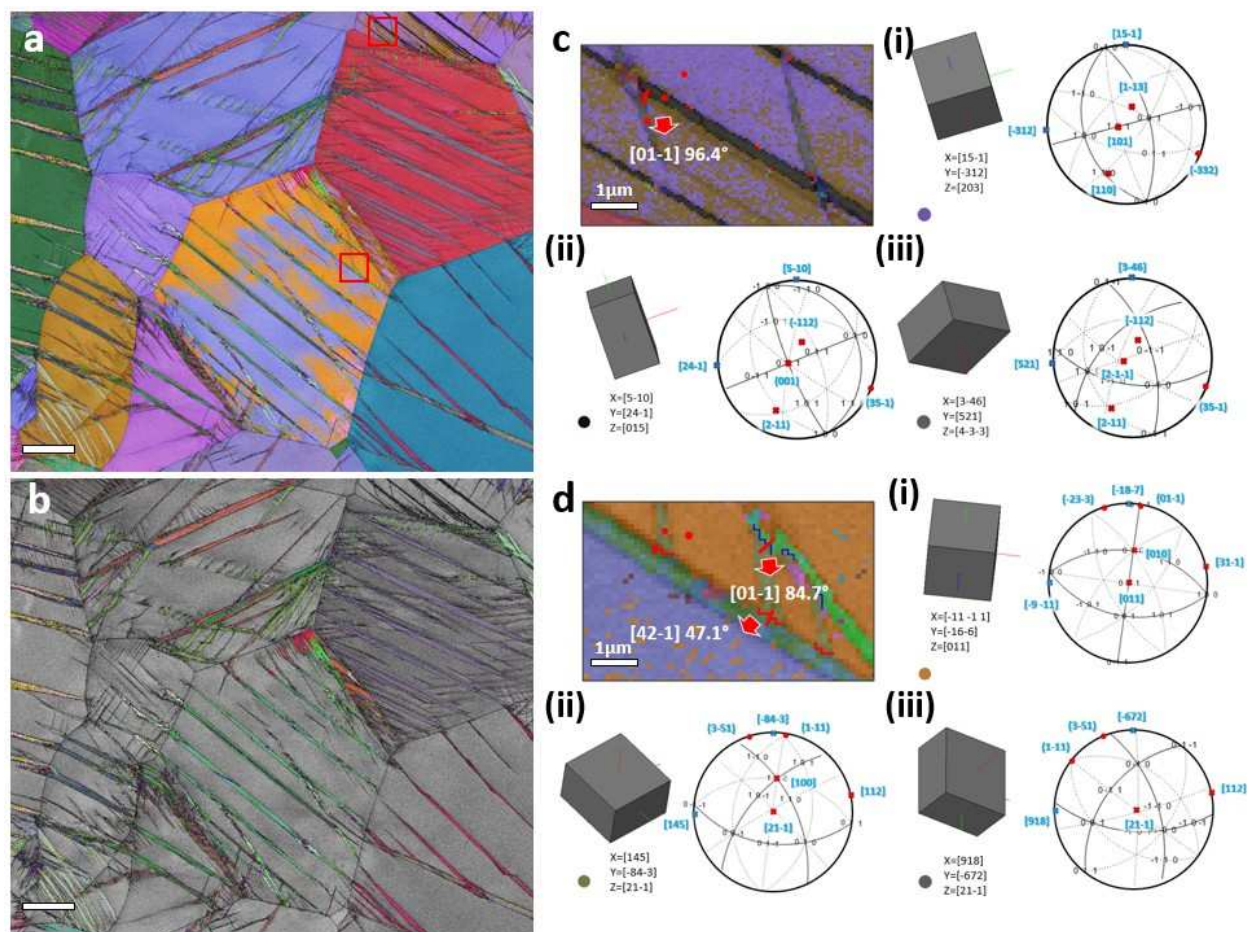
Supplementary Figure 1: Noise-filtered EBSD maps of (TiZrHf)$_{87}$Ta$_{13}$ subjected to 3% deformation. (**a**) Euler angle map of the deformed sample. The indexed martensite phase constitution is confirmed as 6.7%. (**b**) Euler angle map of martensite phase. The insets are martenstic SA twinning feature used for indexation. (**c**) Orientation relationship of the highlighted martensite variants (top red box in (a)). The crystal orientation data is acquired at the red spots. Stereographic projections are generated from the orientation data. The normal axes are (i) [203]$_\beta$ for the β matrix, (ii) [015]$_{\alpha''}$ and (iii) [4-3-3]$_{\alpha''}$ for the primary and {351}<-211>$_{\alpha''}$ type II twinned martensite respectively. (**d**) Orientation relationship of highlighted martensite variants (bottom red box in (a)). The crystal orientation data is acquired at the red spot. Stereographic projections are generated from the orientation data. The normal axes are (i) [011]$_\beta$ for the β matrix, (ii) [21-1]$_{\alpha''}$ and (iii) [21-1]$_{\alpha''}$ for the primary and {351}<-1-12>$_{\alpha''}$ compound twinned martensite respectively. Scale bars, 20μm.
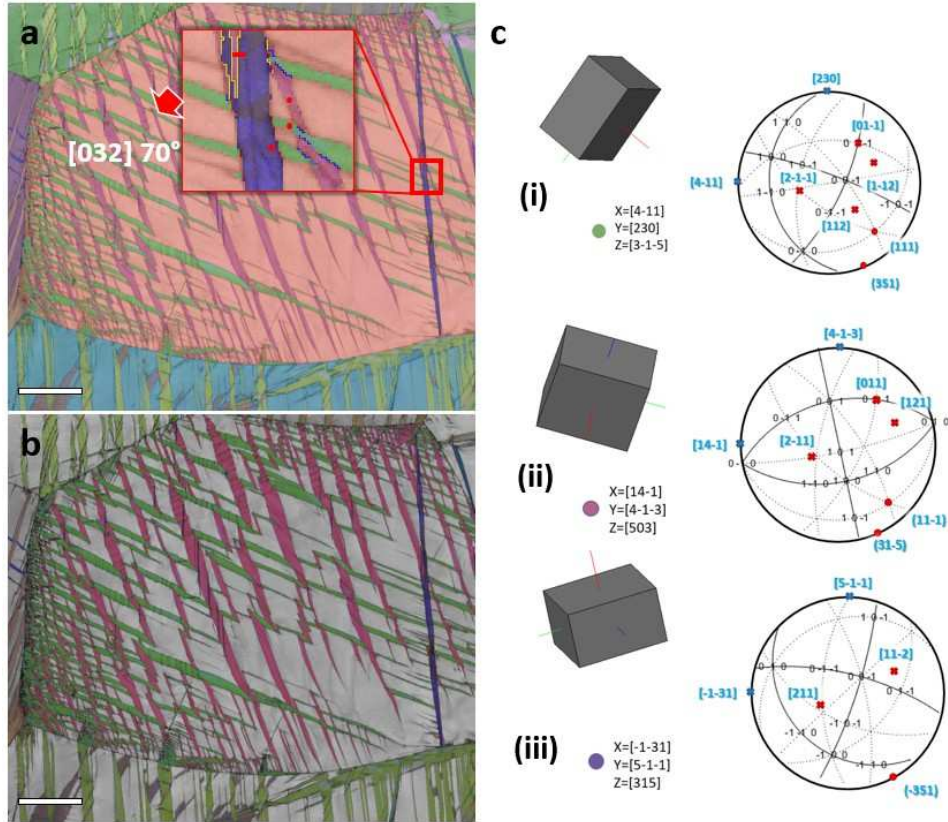
**Supplementary Figure 2: Noise-filtered EBSD maps of (TiZrHf)$_{87}$Ta$_{13}$ subjected to 6% deformation.** (**a**) Euler angle map of the deformed sample. The indexed martensite phase constitution is confirmed as 34.78%. (**b**) Euler angle map of martensite phase. (**c**) Orientation relationship of the highlighted martensite variants (top red box in (a)). The crystal orientation data is acquired at the red spots. Stereographic projections are generated from the orientation data. The normal axes are (i) [3-1-5]$_{\alpha''}$ for α'' matrix, (ii) [503]$_{\alpha''}$ for {111}$_{\alpha''}$ type I twinned variant (iii) [315]$_{\alpha''}$ for α'' {351}<1-12>$_{\alpha''}$ compound twinned variant. Scale bars, 10μm.
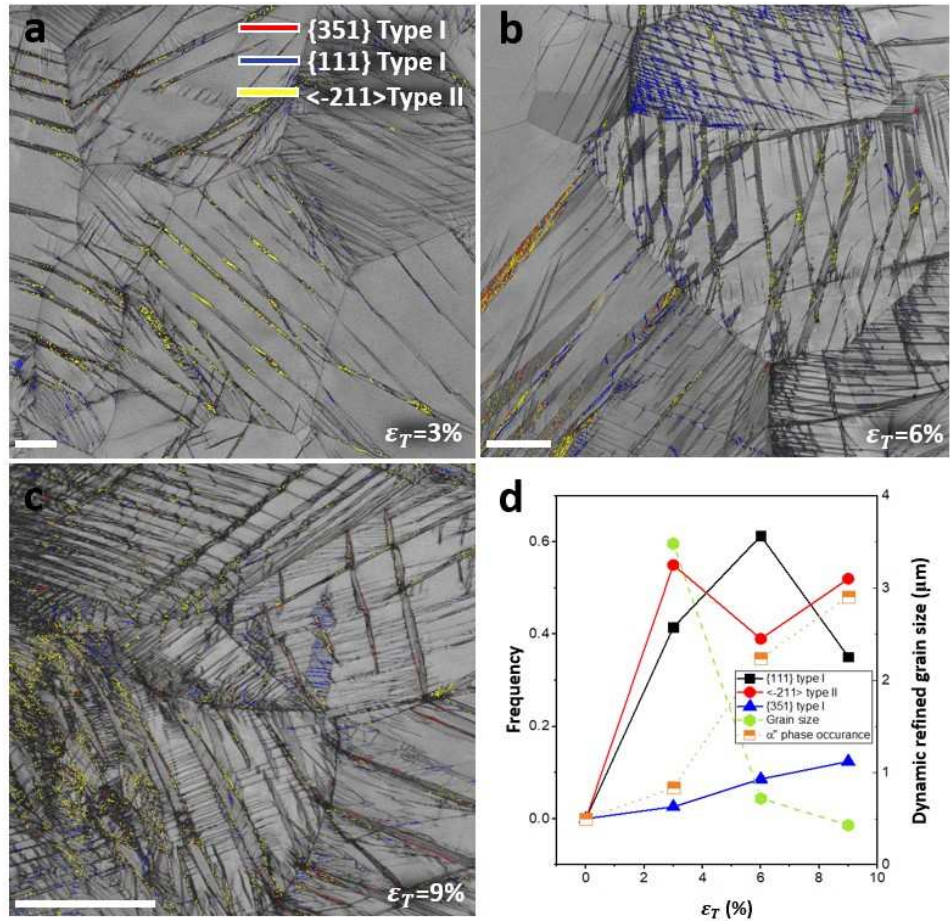
Supplementary Figure 3: Twinning distribution of Ti13 alloy at different strains. (**a-c**) EBSD band contrast map of ε_T=3%, 6%, 9% strained sample. The blue, yellow and red lines represent twinning boundaries of $\{111\}_{\alpha''}$ type I twin, $\{211\}_{\alpha''}$ type II twin and $\{351\}<1\text{-}12>_{\alpha''}$ compound twin respectively. (**d**) Twinning distribution, α'' phase occurrence frequency and dynamic refined grain size at different strain (ε_T=3%, 6%, 9%). Scale bars, 10μm.
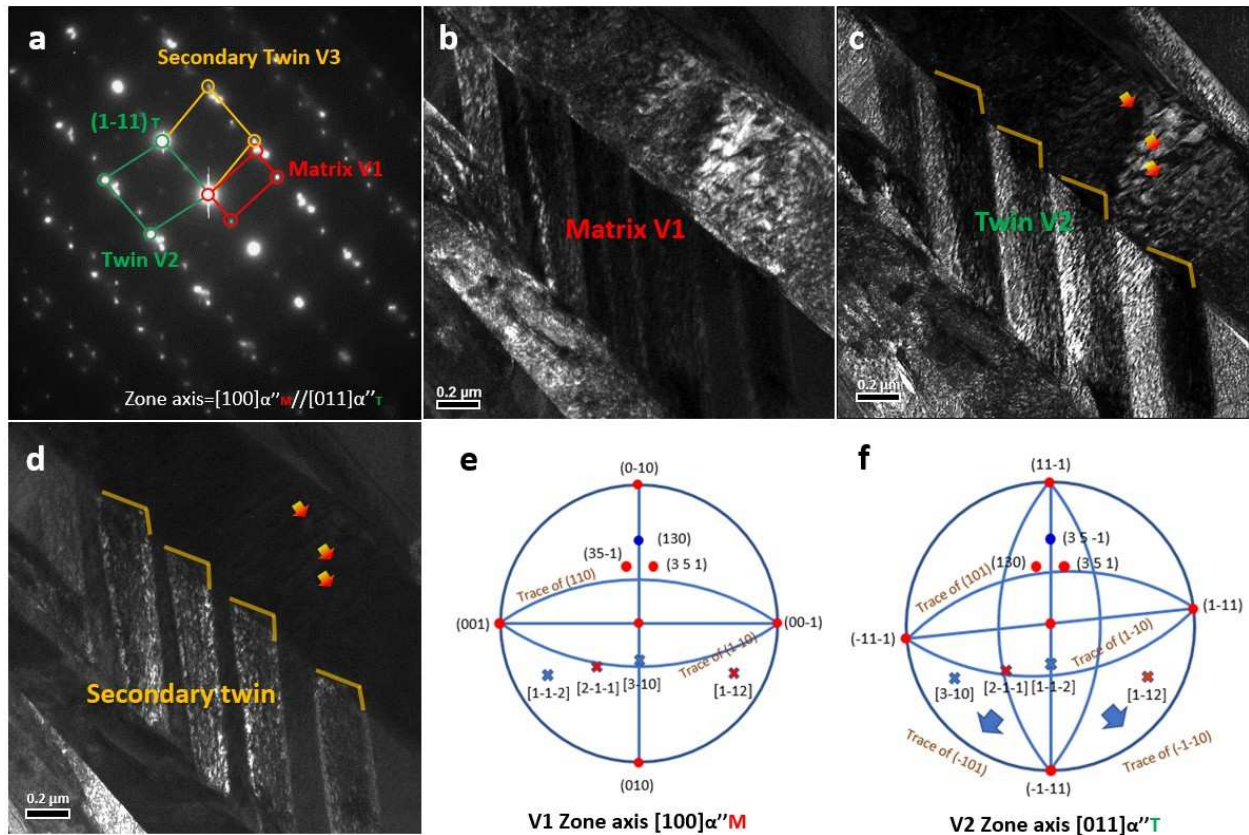
Supplementary Figure 4: Re-tilted {351}<-211>$_{\alpha''}$ Type II twin (**a**) SADP of {351}<-211>$_{\alpha''}$ Type II twin (same area of Figure.2) viewed along [100]$_{\alpha''M}$//[011]$_{\alpha''T}$ zone axis. (**b**) DF image of the α'' matrix V1. (**c**) DF image of the {351}<-211>$_{\alpha''}$ type II twinned α'' V2. (**d**) DF image of the secondary {111}$_{\alpha''}$ type I twinned α'' V3. (**e-f**) Schematic stereographic projections figure constructed for [100]$_{\alpha''M}$ V1 and [011]$_{\alpha''T}$ V2, the special lattice correspondence: (351)$_{\alpha''M}$//(351)$_{\alpha''T}$, (35-1)$_{\alpha''M}$//(130)$_{\alpha''T}$, (130)$_{\alpha''M}$//(35-1)$_{\alpha''T}$ are highlighted. Scale bars, 0.2μm.
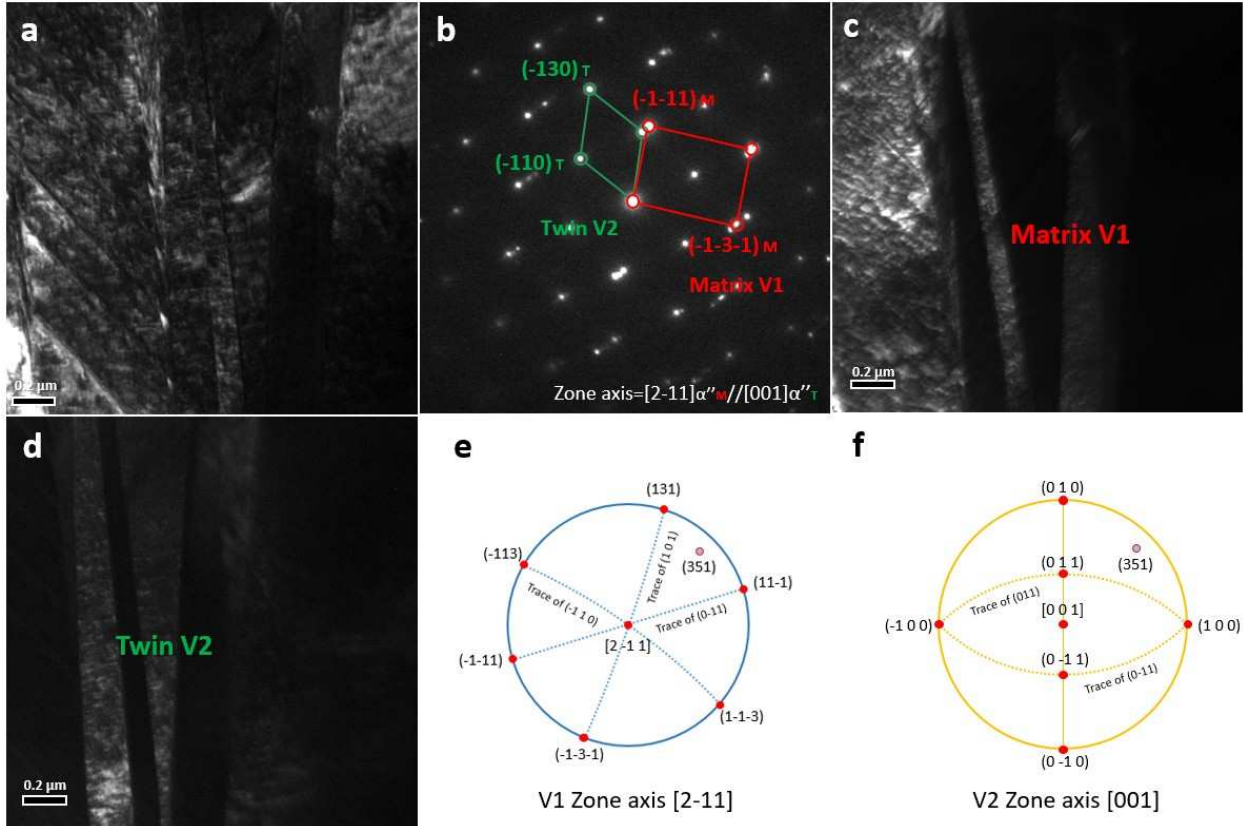
**Supplementary Figure 5: Re-tilted {351}<-211>_α'' Type II twin** (**a**) BF image of re-tilted {351}<-211>_α'' type II martensite twin (same area of Figure.2). (**b**) SADP of {351}<-211>_α'' type II matrix and twinned variant taken along the $[2\text{-}11]_{\alpha''M}//[001]_{\alpha''T}$ zone axis. (**c**) DF image of the α'' matrix V1. (**d**) DF image of the twinned α'' V2. (**e**) Schematic stereographic projections figure constructed for $[2\text{-}11]_{\alpha''M}$ and $[001]_{\alpha''T}$ with highlighted $(351)_{\alpha''M}//(351)_{\alpha''T}$ lattice correspondence. Scale bars, 0.2μm.
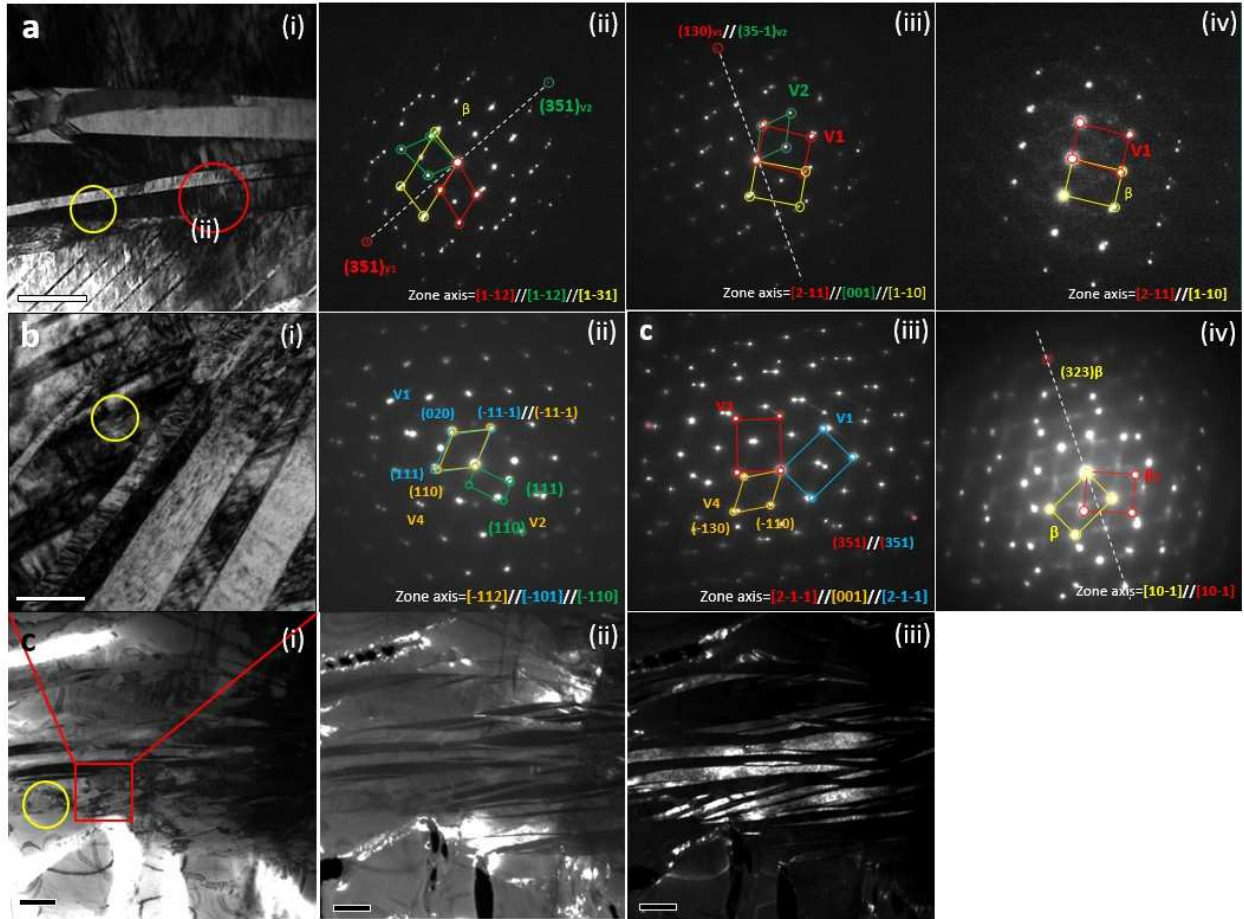
Supplementary Figure 6: SADP comparison of {351}<-211>$_{\alpha''}$ type II and {351}<1-12>$_{\alpha''}$ compound twin under different zone axis. (**a**) Type II SA {351}$_{\alpha''}$ twin in a specimen deformed to 5% strain. **i**. BF image. **ii-iv** Corresponding SADPs taken next to the twin boundary (red circle) along the [1-12]$_{\alpha''V1\&V2}$//[1-31]$_{\beta}$ and [2-11]$_{\alpha''V1}$//[001]$_{\alpha''V2}$//[1-10]$_{\beta}$ zone axis respectively. (**b**) Compound {351}<1-12>$_{\alpha''}$ twin in a specimen deformed to 10% strain. **i**. BF image. **ii-iv** Corresponding SADPs taken next to the twin boundary (red circle) along the [-101]$_{\alpha''V1}$//[-110]$_{\alpha''V2}$//[-112]$_{\alpha''V4}$, [2-1-1]$_{\alpha''V1}$//[2-1-1]$_{\alpha''V3}$//[001]$_{\alpha''V4}$; yellow area in (c) along [10-1]$_{\beta M}$//[10-1]$_{\beta T}$ zone axis respectively. (**c**) Low magnified BF image of the twin feature observed in (b). Red circled area is the feature in (b). (**ii-iii**) DFI of the matrix and twin, taken from reflection observed in b(iv). Scale bar in a, 200nm. Scale bar in b, 50nm. Scale bars in c (i-iii), 500nm.
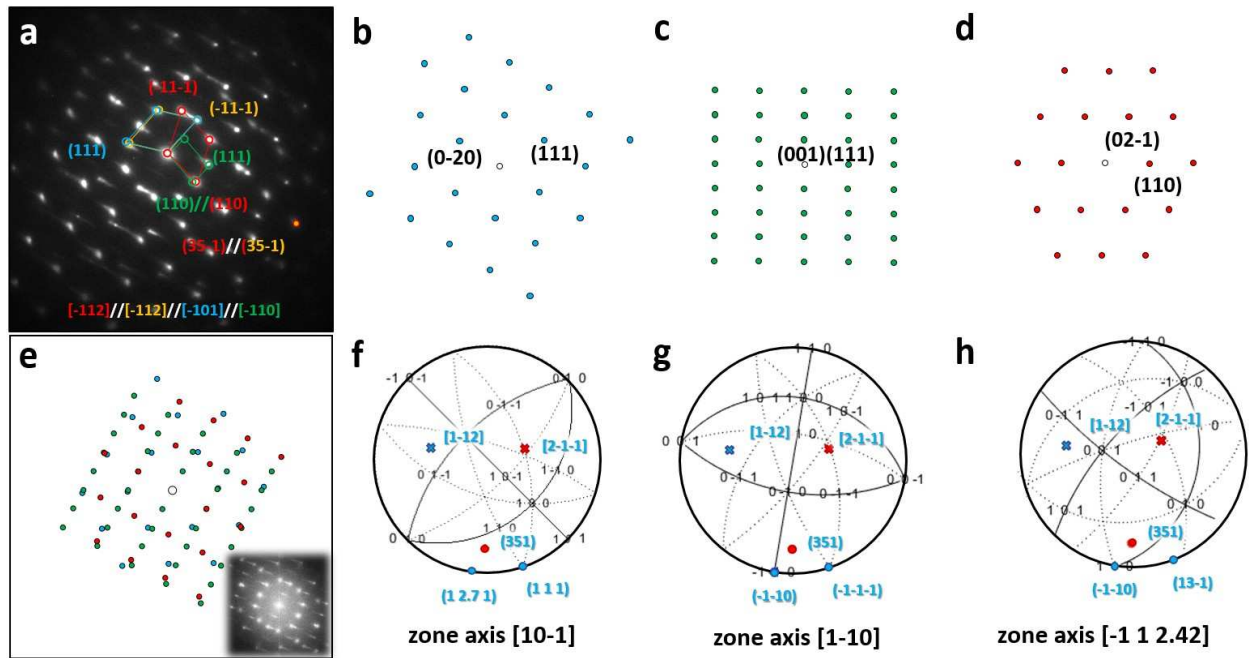
Supplementary Figure 7: OR analysis of {351}<1-12>_{α''} compound twin (**a**) SADP of {351}<1-12>_{α''} compound twin (same as Figure.3(b)) taken along the [-101]_{α''V1}//[-110]_{α''V2}//[-112]_{α''V3&V4} zone axis. (**b-d**) Simulated diffraction pattern of [-101]_{α''V1}, [-110]_{α''V2} and [-112]_{α''V3&V4}. (**e**) Simulated SADP whose DPs arrangement is following FFT of Fig.4a. Showing (111)_{α''V1}//(111)_{α''V2}, (110)_{α''V2}//(110)_{α''V3}. (**f-h**) Stereographic projections of V1-V3, generated from the orientation data in (e). The special lattice correspondence: (351)[1-12][2-1-1]_{α''V1}//(351)[1-12][2-1-1]_{α''V2&v3} are highlighted.
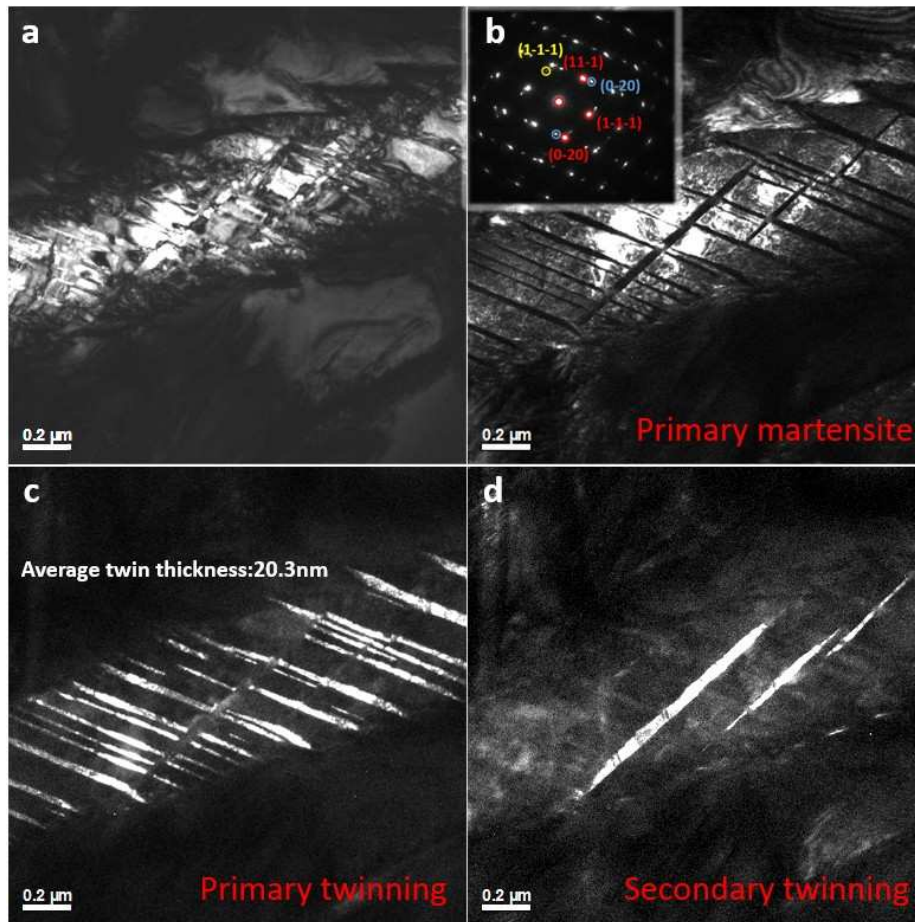
Supplementary Figure 8: TEM image of fine multimodal martensite twin in a specimen subject to 10% strain. (**a**) BFI of $\{111\}_{\alpha''}$ type I multimodal twinning microstructure. (**b**) DFI of primary martensite. The inset is a SADP taken along the $[101]_{\alpha''}$ zone axis, where three martensite variants are marked by red, blue and yellow circles. (**c**) DFI of primary $\{111\}_{\alpha''}$ twinning. The average twin thickness is measured to be 20.3nm. (**d**) DFI of secondary $\{111\}_{\alpha''}$ martensite twin. Scale bars, 0.2μm.
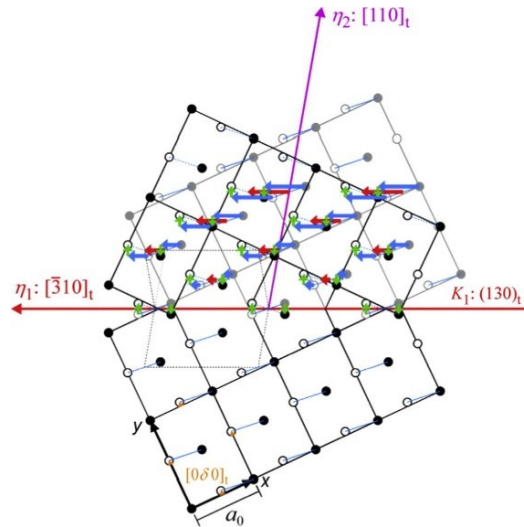
Supplementary Figure 9: Illustration of atomic shuffle in martensitic twinning. $(001)_{\alpha''}$ Projection of the $(130)[3\text{-}10]_{\alpha''}$ twinning in the tetragonal structure (δ is atomic displacement along $[010]_{\alpha''}$). Closed circles represent atoms in the projection plane, and open circles are atoms $0.7071a_0$ above or below the projection. The red arrows indicate the shear of the lattice points. The blue lines and arrows indicate the motif units and the shear of the atoms comprising the units, respectively. The green arrows indicate the shuffle.
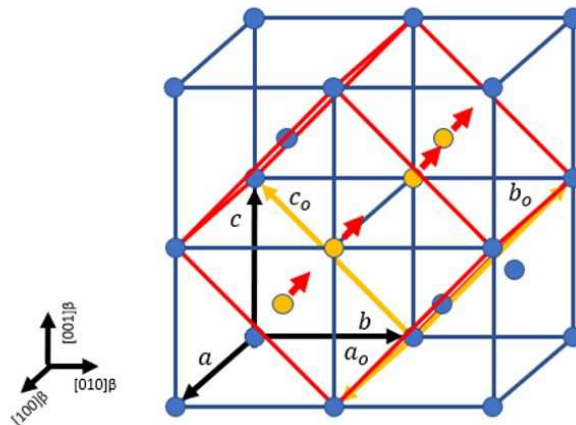
Supplementary Figure 10: Lattice correspondence of six martensite(base centered orthorhombic, red lattice) in BCC (blue lattice) matrix. Red arrows indicates the lattice instability of $\{001\}<010>_{\alpha''}$ induced atomic shuffle.

Supplementary Tables

Supplementray Table I. Misorientation profile of identified martensitic twinning.

Twinning modes	Misorientation axis	Angle
$\{111\}_{\alpha''}$ type I twinning[42]	$<011>_{\alpha''}$	85°
$<2\text{-}1\text{-}1>_{\alpha''}$ type II twinning[42]	$<011>_{\alpha''}/<032>_{\alpha''}$	96.4°/70°
$(351)<1\text{-}12>_{\alpha''}$ compound twinning	$<42\text{-}1>_{\alpha'''}$	47.1°

Supplementray Table II. Lattice correspondence between different crystallographic operations on the frame of the $(351)<2\text{-}1\text{-}1>_{\alpha''}$ type II twin.

Twinning operation	Main target zone axis correspondence of α'' twins					
Matrix	<1 0 0>	<001>	<10-1>	<1-12>	<2-11>	<1-10>
$(351)<2\text{-}1\text{-}1>_{\alpha''}$ type II twin	<0 1 1>	<2-11>	<1-10>	<-11-2>	<001>	<10-1>
$(351)<1\text{-}12>_{\alpha''}$ compound twin	<2 -7 -1.4>	<-0.3 -0.2 1>	<1 -1 -2.4>	<1-12>	<-88-5>	<3-10>
$(130)<3\text{-}10>_{\alpha''}$ mechanical twin	<6 -5 0>	<001>	<6 -5 -10>	<1.7 0 2>	<2.3 -0.5 1>	<1.7 0.1 0>

Supplementary Table III. Possible martensitic twinning modes with rational K_1 and η_2 elements.

Possible twinning modes	K_1	η_1	K_2	η_2	s
{130}<3-10> Compound	{130}	<-310>	{-110}	<110>	0.3536
{351}<1-12> compound	{351}	<1-12>	{1-13}	<110>	0.3536
<211> type II Mode 3	{3-5-1}	<211>	{111}	<6-5-1>	0.1405
<211> type II Mode 2	{-13-1}	<211>	{111}	<-23-1>	0.0787
<211> type II Mode 1	{1-1-1}	<211>	{111}	<2-1-1>	0

Supplementary Notes

Supplementary Note I: Lattice correspondence

In current study, to cacluate the lattice correspondence betwwen different α'' twinned variants and β matrix. The following lattice correspondance relationship was taken (through undeformed base centred orthorhombic coordinate):

Body centric cubic	a [1 0 0]	**b [0 1 0]**	**c [0 0 1]**
Orthorhombic	a_0 [1 0 0]	b_0 [0 ½ -½]	c_0 [0 ½ ½]

For clearance the twinning elements calculation and lattice correspondence determination are all conducted on the undeformed base centred orthorhombic lattice (Supplementary Fig. 10).

Supplementary Note II: Twinning evolution analysis

We derive the misorientation profile for the three types of twinning from the EBSD result shown in Fig. 1b. Stereo-projection figures were constructed for all observed twinning systems. A special case is confirmed in Supplementary Fig. 3 where the misorientation angle of the $\{111\}_{\alpha''}$ type I twinned α''variant is exhibit $<032>_{\alpha''}$~70° with the $\{351\}<1\text{-}12>_{\alpha''}$ compound twinned variant. With $<211>_{\alpha''}$ in Supplementary Fig. 2c(ii) superimposed on Supplementary Fig. 2c(iii), this misorientation profile was considered as a special type II $<211>_{\alpha''}$ twin. We calculated the twinning distribution under 5° threshold, α'' occurrence and dynamic refined grain size of different strain level based on the EBSD results in Fig. 2b. The results are summarized in Supplementary Figure. 3.

Methods

Sample preparation

The compositions of the alloy investigated in the current work is $(TiZrHf)_{85}Ta_{15}$ and $(TiZrHf)_{87}Ta_{13}$. The ingots of these alloys with a mass of 10g were synthesised by arc melting the respective elements (purities higher than 99.9wt%) in a Ti-gettered high-purity argon atmosphere (Edmund Buhler MAM 1 arc-melter, German). Ingots were re-melted three times for homogeneity. Ingots were then arc-melted and drop-cast through a water-cooled copper cast moulds to produce rods with diameter of $5 \times 5 \times 80mm$. Sample rods were then sealed in quartz tube which has been pre-vacuumed and fulfilled with high purity argon. Samples were then homogenized in furnace under 1473K for 2 hr and quenched in water. After cold rolled with reduction around 70%, the rods surface was grinded down to 2000 grin size to remove oxidation and re-sealed in quartz tube under same conditions. After annealed at 1123K for 0.5 hr, the rods were subsequently quenched in water and machined by electrical discharge machining (EDM) for dog bone tensile sample following ASTM E8/E8M-13(subsize) standard. The tensile tests were then performed on a ZWICK Z050TH materials testing system with a strain rate of 4×10^{-4} s^{-1}. The oxygen content analysis was performed by AMG analytical service through wet chemical method, the final oxygen content is confirmed as 0.12%(wt). X-ray diffraction (XRD) was used for primary determination of phase constituents for all samples tested. The post-test sample were sectioned into 3 mm × 2 mm x 1 mm thick coupon (cross section area) for XRD analyses. All samples were polished up to 1 μm using diamond suspension. All samples for scanning electron microscopy (SEM), electron back scattered diffraction (EBSD) were prepared by mechanical polishing. Coarse grinding was undertaken with silicon carbide grinding paper ranging from P120 to P4000. Water-based diamond suspension with sizes from 9 μm to 1 μm were used for primary polishing. Fine polishing was conducted with 0.06 μm alumina suspension with H_2O_2 (30% solution) addition with the ratio of 1:20. All samples were then ion polished with a Gatan PECS II ion polishing system under a 3keV condition for 5 minutes to remove possible contamination and residue chemical suspension. TEM samples were prepared by sectioning tensile samples into 3 mm × 3 mm × 1mm sections and grinding to 90 μm thickness followed by twin-jet electropolishing. The electropolishing was performed by the Struers TenuPol-5 twin-jet electropolishing system with a solution of 5% perchloric acid, 35% 2-butoryethanol and 60% methanol. The samples were then put into a Gatan Precision Ion Polishing (PIPS II) system for a final clean at 0.3 kV for 5 min.

Microstructure and twinning characterization

XRD tests were conducted on a Bruker D2 Phaser with Cu-K$_\alpha$ radiation source. The characterisation of XRD for the primary phase was performed by TOPAS[52] code was then utilised for Rietveld refinement to identify accurate lattice parameters and phase constituents. The microstructural characterisation of the deformed samples were performed on a FEI Inspect F50 FEGSEM using a 20 kV accelerating voltage which fitted with an Oxford Instruments EBSD detector. Quantitative processing was completed using HKL's Channel5 EBSD post-processing software. The deformation mechanisms and microstructural evolution of samples were analysed by transmission electron microscopy (TEM). Various TEM instruments were utilised to investigate the microstructure and evolution deformation mechanisms of the tested samples. For low magnification imaging and selected area diffraction patterns (SADP), a FEI Tecnai 20 TEM with an accelerating voltage of 200kV were used. High-resolution microstructural characterisation was performed on a Titan 80/300 and JEOL-R005 Cs aberration corrected HRTEM with an accelerating voltage of 300kV. All TEM images were primarily post-processed with Gatan digital micrograph software. The SADP indexation was accomplished with CrysTBox[53], PTCLab[54] and MATLAB.